

Article

Interannual Variability in the Coastal Zones of the Gulf of California

Emilio Palacios-Hernández ^{1,*}, Jorge Manuel Montes-Aréchiga ¹, Luis Brito-Castillo ², Laura Carrillo ³, Sergio Julián-Caballero ¹ and David Avalos-Cueva ⁴

¹ Physics Department, University of Guadalajara, 1500 Revolución, Olímpica Sector, Guadalajara 44430, Jalisco, Mexico; jorge.montes@academicos.udg.mx (J.M.M.-A.); sergio.julian9245@alumnos.udg.mx (S.J.-C.)

² Centro de Investigaciones Biológicas del Noroeste SC, Unidad Guaymas, Guaymas 85454, Sonora, Mexico; lbrito04@cibnor.mx

³ Departamento de Observación y Estudios de la Tierra, El Colegio de la Frontera Sur, la Atmósfera y el Océano, Av. Centenario km 5.5, Col. Pacto Obrero, Chetumal 77014, Quintana Roo, Mexico; lcarrillo@ecosur.mx

⁴ Department of Civil Engineering and Topography, University of Guadalajara, 1421 Blvd. Marcelino García Barragán, Guadalajara 44430, Jalisco, Mexico; david.avalos@academicos.udg.mx

* Correspondence: emilio.palacios@academicos.udg.mx

Abstract: Few studies have explored the details of climatology in the Gulf of California (GoC) coastal zone, a region characterized by robust land–sea breeze circulation that results from land heating on both coasts of the GoC. Using hourly historical observations from automatic weather stations (AWSs) from 2008 to 2018, we performed harmonic and empirical orthogonal function analyses to describe the climatology of several characteristics that are regularly monitored in the GoC coastal zone. The characteristics included air temperature (°C), relative humidity (%), atmospheric pressure (hPa), wind intensity (m s^{-1}), and wind direction (°). The National Water Commission (CNA) provided records for stations located along the coast of the GoC. The results revealed an intense annual and, to a lesser extent, interannual signal for all characteristics. The presence of synoptic patterns forces seasonal and intraseasonal variations to occur. In summer, tropical systems increase the seasonal variability, mainly at the eastern mouth of the GoC. Some stations display this increase until the cold season arrives with the passage of winter systems. Finally, we found that interannual variability could be associated with El Niño–Southern Oscillation events.

Keywords: interannual; El Niño–southern oscillation; gulf of California; coast; seasonal and intraseasonal variability



Citation: Palacios-Hernández, E.; Montes-Aréchiga, J.M.; Brito-Castillo, L.; Carrillo, L.; Julián-Caballero, S.; Avalos-Cueva, D. Interannual Variability in the Coastal Zones of the Gulf of California. *Climate* **2023**, *11*, 132. <https://doi.org/10.3390/cli11060132>

Academic Editor: Forrest M. Hoffman

Received: 20 April 2023

Revised: 13 June 2023

Accepted: 15 June 2023

Published: 17 June 2023



Copyright: © 2023 by the authors. Licensee MDPI, Basel, Switzerland. This article is an open access article distributed under the terms and conditions of the Creative Commons Attribution (CC BY) license (<https://creativecommons.org/licenses/by/4.0/>).

1. Introduction

The Gulf of California (GoC) is a semienclosed sea in northwestern Mexico. It supports remarkable biodiversity and is one of Mexico's most important fishing areas. Throughout the year, the GoC coastal zone is exposed to several transient weather phenomena, such as cold fronts, troughs, high-pressure systems, the Mexican monsoon, and tropical systems (i.e., mesoscale convective systems (MCSs) and tropical cyclones [1–4]). Seasonal variations in rainfall, thunderstorms, wind field, pressure, moisture, and air temperature along the coasts of the GoC are influenced by interannual patterns such as ENSO (El Niño–Southern Oscillation; [5–14]) and decadal modes of PDO (Pacific Decadal Oscillation; [15–17]) and AMO (Atlantic Multidecadal Oscillation; [8,18,19]).

Despite the high productivity and economic importance of the GoC, few studies have been conducted to explore the details of the coastal zone's climatology. Some studies explored the structure of wind fields over the gulf and the surrounding areas [20–22] to elucidate the characteristics of the diurnal cycle of the winds. Others explored the moisture flux transport from the Pacific Ocean into the southwestern United States and Mexico [23–25] through the

GoC to describe the convective activity inland, suggesting a connection between surges and severe thunderstorms over the marginal regions of the monsoon.

For instance, Ciesielski and Johnson [26] analyzed wind surface observations from different sources, concluding that land heating on both coasts of the GoC results in robust land–sea breeze circulation. Simultaneously, Brito-Castillo, Alcocer-Vázquez, and Félix-Domínguez [20] described the seasonal and daily variations in winds in Sonora, including the coastal zone of the GoC, indicating that changes manifest marked seasonality. Bordoni and Stevens [22], performing a principal component analysis of the summer near-surface time quick scatterometer, found an index for gulf surge occurrence based on the daily variability in the alongshore winds over the GoC. Apart from wind observations, other weather characteristics have not been studied in detail because of the lack of long-term subdaily measurements. The need to calculate the climatology of several variables results from the urgency of knowing the trends observed under the global warming hypothesis [27]. Ripple et al. [28] claim that the world is already facing unprecedented climate disasters.

For instance, Wang and Toumi [29] found that in the last two decades, the tropical cyclone maximum intensity tended to occur closer to land relative to that in previous decades, indicating increasing global concern for coastal areas that could be affected by aggravated extreme weather. Tropical cyclones affect the weather of the GoC, particularly in September, when they reach their northernmost position and may occasionally enter the gulf, influencing the coastal zone and causing severe weather. Moreover, tropical storms, such as mesoscale convective systems, can move across the GoC from a region of deep convection over and off the coast of Nayarit [1], implying that high winds and heavy rainfall are part of the warm season climatology of the GoC, including extremely high temperatures. Therefore, there is also a concern about their deviations from current routines and potential future changes. Nevertheless, to calculate deviations from averages, it is necessary to know the value of the long-term mean (i.e., the climatology).

Although subdaily observations in the GC coastal zone only span a few years, it is possible to roughly estimate the climatology of typical monitored characteristics in the GoC coastal zone. This calculation requires the exploration of all possible high-quality available data. In an attempt to overcome the difficulty of constraining the climatology of different weather features with a subdaily temporal resolution, in this work, we analyzed eleven years (2008–2018) of ground observations from the AWS network located along the GoC coast (Figure 1). The variables that were analyzed at an hourly temporal resolution were wind direction and speed (WD, WS), air temperature (AT), relative humidity (RH), and atmospheric pressure (AP). Eight out of thirty coastal station networks with at least ten years of data from 2008 to 2018 were selected, and the stations displayed maximum spatial coverage. The results can be used to explore the effect of interannual events on climatology and elucidate their possible teleconnections with other large-scale phenomena.

The Gulf of California

The GoC is a narrow strip of water in northwestern Mexico, delimited by the Baja California Peninsula and continental Mexico, from 22°52' N to 31°45' N, oriented in a northwest–southeast direction. It is considered a subtropical inland sea with a length of 1100 km, a width of 80 to 240 km, and a surface area of approximately 160,000 km² (Figure 1). The southern part of the gulf has abrupt submarine topography with depths of up to three kilometers, while the northern part is shallow (400 m).

The ENSO phenomenon significantly impacts the climate in northern Mexico. Its warm phase (El Niño) is related to more significant precipitation in winter. In contrast, the cold phase (La Niña) generally tends to favor the presence of drier winters and more accentuated droughts [10,14,30]. According to Köppen's climate classification, modified by [31], arid conditions dominate along the region with particular characteristics over the continent due to local atmospheric phenomena and a mountain range that isolates it from the influence of the ocean. The climate of the region is arid (classified as BW) and divided into three climate subtypes, mainly according to the degree of rainfall and temperature.

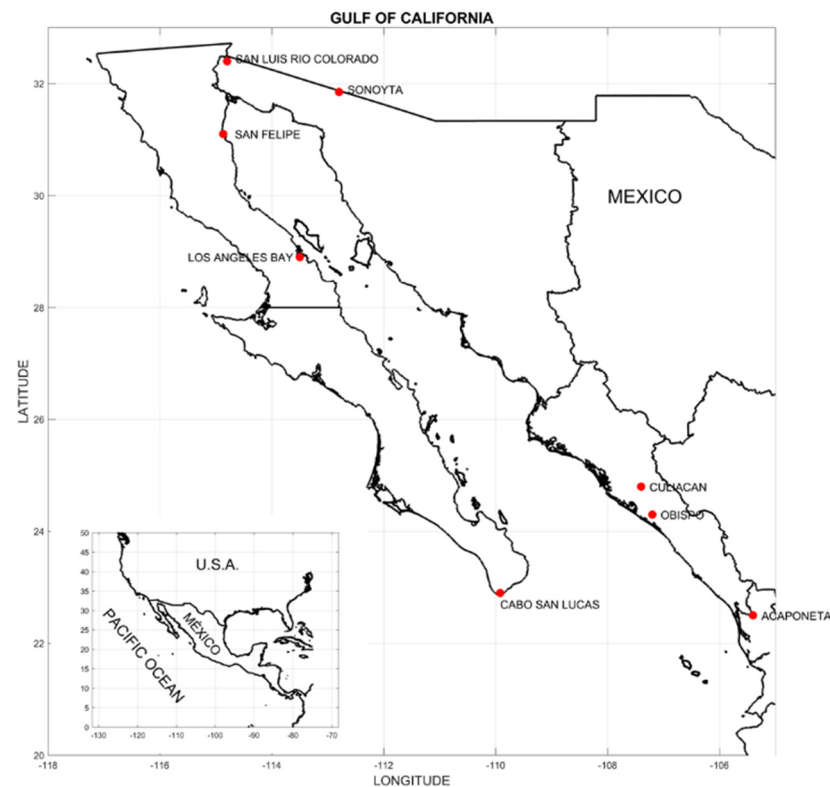


Figure 1. Gulf of California showing automatic weather stations (AWSs).

In winter, several midlatitude systems predominate, such as cold fronts, air masses, and jet streams [14,19,30], while in summer, rainfall is primarily controlled by the North American monsoon (NAM) system [16,32–36] and numerous transient disturbances, such as mesoscale convective systems, tropical cyclones, easterly waves, inverted troughs, the Madden Julian oscillations, and midlatitude troughs. Wang and Fiedler [37] noted that ENSO is a coupled phenomenon in the ocean–atmosphere system that causes climate variability in the GoC. Bernal et al. [38] compared the time series of sea surface temperature (SST), wind speed, and rainfall in the southern GoC with two climate indexes, the El Niño–Southern Oscillation (ENSO) and the North Pacific Interdecadal Oscillation (NPIO), finding that the most significant forcings come from the tropical and equatorial Pacific and that the North Pacific influences wind behavior and, to a lesser extent, SST and precipitation.

In summer, the Sonoran Desert, which extends northward across the international boundary into the United States [39,40], receives significant humidity from the tropical Pacific Ocean. Monsoon circulation has been detected at the surface (450 m), with atmospheric flows from the east coming from the Gulf of Mexico and the Eastern Tropical Pacific Ocean, producing a convergence over the Sierra Madre Occidental and the Sonoran Desert [34,41].

2. Data Processing and Methods

2.1. Data

Hourly observations of air temperature (AT, °C), relative humidity (RH, %), atmospheric pressure (AP, hPa), wind (W, m/s) and zonal (U, east–west m/s) and meridional wind (V, north–south, m/s) components were covered during the period from 1 January 2008 to 31 December 2018. The National Water Commission (CNA) provided data from 30 automatic weather stations (AWSs). We selected eight AWSs that compiled at least eleven years of continuous recording (Table 1). Monthly means were calculated for each variable.

Table 1. Information on eight automatic weather stations (AWSs).

	Number-Station	Label	Altitude (m)	Latitude (N)/ Longitude (W)
1.	Cabo San Lucas	CLS	35	22°54'00.52" / 109°55'00.12"
2.	Bahía de los Angeles	BLA	4	28°57'07.68" / 113°33'44.83"
3.	San Felipe	SFL	15	31°01'34.50" / 114°50'29.37"
4.	San Luis Río Colorado	SRC	42	32°27'08.89" / 114°46'17.88"
5.	Sonoyta	SNY	389	31°56'48.20" / 112°45'55.77"
6.	Culiacán	CLC	60	24°48'54.73" / 107°23'51.94"
7.	Obispo	OBP	37	24°17'32.84" / 107°09'31.93"
8.	Acaponeta	ACP	24	22°28'04.59" / 105°23'02.72"

The missing values were estimated by generating a monthly canonical year from the eleven-year records, which followed the arithmetic mean for each variable's hourly, daily, monthly, and annual average.

$$AC = \frac{X_1 + X_2 + X_3 + \dots + X_N}{N}, \quad (1)$$

where $X_1 + X_2 + X_3 + \dots + X_N$ is the observation set of any weather variable and N is the number of observations. Diurnal and semidiurnal variations were removed via a filtering procedure, as described in [13].

2.2. Harmonic Analysis

Weather features display harmonic behavior because seasonal trends are repeated year after year. We used the harmonic analysis method proposed by Ripa [42] to establish the seasonal climatology of the GoC coastal zone. This method is widely used in many other works ([43,44], among others). In addition to establishing a canonical year, the harmonic analysis method was used to fill in the gaps in the observations. Harmonic analysis was applied to the monthly mean of each variable to obtain the annual, semiannual, and other periods' amplitude and phase, which can be expressed as follows:

$$X_{(t_n)} = \bar{x}(t) + \sum_{i=1}^M C_i \cos(\omega_i t_n - \varphi_i) + x_r(t_n), \quad (2)$$

where $X_{(t_n)}$ is the observation in an instant of time; $\bar{x}(t)$ is the mean value of the original time series; C_q , ω_q y φ_q are the amplitude, frequency, and phase of the q-th component, respectively; and $x_r(t_i)$ is the residual component.

2.3. Empirical Orthogonal Functions

After confirming the results obtained via the harmonic analysis, we performed an empirical orthogonal function (EOF) analysis. The EOF analysis indicated the interannual events (e.g., ENSO) that affected the study area. The EOF transformed the time series in terms of orthogonal functions or statistical modes that explained most of the variance in the original data set. Only the modes that explained most of the variance were considered.

The EOF can be represented as

$$Z(x, y, t) = \sum_{k=1}^n PC(t) \cdot EOF(x, y), \quad (3)$$

where $Z(x, y, t)$ are the data series to be analyzed, $EOF(x, y)$ represents the spatial structure of the k -th factor that explains variation over time, and $Z, PC(t)$ is the principal component that explains the temporal amplitude of each EOF .

2.4. Spectral Analysis

The spectral analysis of the temporal modes of the EOFs was used to establish the most energetic frequencies in those modes and thus establish the corresponding climatology. The series in the time–frequency space were decomposed by employing a Fourier transform. Spectral analysis is used in many studies and is expressed as follows:

$$ZC_x(\omega) = \sum_{n=1}^N x_n e^{-i2\pi\omega t_n} \Delta t, \quad (4)$$

where x_n is a time series, N is the total length of the series, Δt is the sampling interval, and ω is the frequency; the power spectral density is then obtained as follows:

$$S_{xx}(\omega) = \frac{1}{T} C_x(\omega) \cdot C_x^*(\omega), \quad (5)$$

2.5. Interpolation

To visualize the spatial fields of harmonic analysis and the spatial modes of the EOFs, it was necessary to interpolate the spatially irregular fields into a regular grid. The harmonic analysis and spatial EOF modes were displayed with surface maps created with the kriging interpolation method to provide the best linear unbiased estimator with minimum variance [45]:

$$Z(x) = m(x) + V(x) + R(x), \quad (6)$$

where $Z(x)$ is the value of the variable Z in the x position; $m(x)$ is the deterministic function describing the structural component associated with the data set, $V(x)$ is the local stochastic variation remaining in the data after removing the structural variation given by $m(x)$, and $R(x)$ is the residual from the variability without a spatial trend and with zero mean and quadratic variance (Appendix A indicates interpolation relative errors, Figure A1).

2.6. Correlation Coefficient

We calculated the correlation between the temporal modes of the EOFs and indexes associated with ENSO events to establish their similarities and to explore the teleconnection between ENSO events and the climatology of the GoC coastal zone.

The correlation between (X and Y) was calculated as follows:

$$\rho(X, Y) = \frac{cov(x, y)}{\sigma_x \sigma_y} = \frac{E((X - \sigma_X)(Y - \sigma_Y))}{\sigma_x \sigma_y}, \quad (7)$$

$cov(x, y)$ is the covariance of σ_X and σ_Y , which are the standard deviations of X and Y , and the correlation value (ρ) varies in the interval $[-1, +1]$.

3. Results

3.1. Harmonic Analysis

Table 2 shows the results of the harmonic analysis, where $A_1, A_2, A_3,$ and A_4 are the annual, semiannual, temporal, and quarterly amplitudes, respectively; $\phi_1, \phi_2, \phi_3,$ and ϕ_4 are the respective phases; and EV is the explained variance. According to Table 2, the highest average AT values were observed in the southeastern part of the study area and corresponded to Acaponeta (25.3 °C) and Culiacan (25 °C). In contrast, the lowest AT was observed in the northeast and corresponded to Sonoyta (23°). The percentage of

variance was ~90%. There were minimal discrepancies in AP values between sites. The highest values were in Cabo San Lucas (1013.4 hPa), in the southernmost portion of the Baja Peninsula.

Table 2. Calculations of the 1st to 4th harmonic for each station, where amplitudes are A_i , phase angles are ϕ_i (months), and explained variance is EV.

	Variable	CSL	BLA	SFL	SRC	SNY	CLC	OBP	ACP
Mean	TEMP. (°C)	24.5	24.3	24.5	24.3	23.0	25.0	24.1	25.3
	A. P. (hPa)	1013.4	1010.4	1009.3	1009.9	1009.2	1009.8	1010.1	1009.4
	R. H. (%)	58.5	42.4	40.5	40.0	37.7	66.8	75.5	71.4
	U (m/s)	−2.19	−7.45	−0.52	−0.27	0.63	−0.80	0.08	−2.02
	V (m/s)	−0.69	−0.60	1.17	1.53	−1.65	−0.68	0.50	0.28
A_1/ϕ_1	TEMP. (°C)	3.69	6.86	7.66	9.69	9.94	5.93	6.32	4.47
		7.7	7.6	7.4	7.1	7.0	7.5	7.8	7.4
	A. P. (hPa)	2.06	4.39	5.30	5.56	4.02	2.12	1.87	1.79
		0.9	1.1	0.8	0.9	0.8	1.2	1.3	1.4
	R. H. (%)	10.57	5.78	10.87	7.67	10.75	3.21	2.0	8.57
		9.3	10.0	8.5	11.7	10.8	10.2	9.5	9.5
	U (m/s)	1.10	0.95	2.00	1.06	2.66	0.25	0.40	2.03
	6.0	0.3	6.7	10.0	0.4	11.7	0.0	10.4	
	V (m/s)	0.56	3.64	0.63	5.43	2.56	1.54	0.29	1.24
		0.0	1.3	1.3	1.0	0.3	11.7	0.0	10.4
A_2/ϕ_2	TEMP. (°C)	0.65	1.29	1.85	2.29	2.19	0.88	0.82	0.82
		3.5	2.5	2.6	2.4	2.5	3.8	3.9	4.4
	A. P. (hPa)	0.60	0.73	0.91	0.55	1.09	0.91	0.65	0.67
		1.2	1.0	0.7	1.0	1.2	1.0	1.2	1.3
	R. H. (%)	4.82	6.65	3.80	4.44	2.74	5.89	3.94	4.61
		1.6	1.9	0.3	1.4	1.0	2.0	2.3	1.9
	U (m/s)	0.82	4.15	0.62	0.59	0.22	0.30	0.22	0.50
	4.4	2.2	1.9	0.6	4.1	2.9	3.1	1.5	
	V (m/s)	1.04	2.03	0.53	2.09	0.78	0.10	0.03	0.28
		4.9	1.9	5.2	4.1	2.1	1.3	5.4	3.1
A_3/ϕ_3	TEMP. (°C)	0.63	0.85	0.56	1.08	0.95	0.95	1.0	1.02
		2.3	2.4	2.6	2.4	2.2	2.1	2.2	1.8
	A. P. (hPa)	0.33	0.42	0.21	0.36	0.27	0.22	0.25	0.36
		3.4	0.0	3.9	3.5	0.1	3.9	3.9	3.6
	R. H. (%)	2.65	1.69	1.61	2.52	4.84	0.48	0.63	1.27
		0.3	0.3	3.4	3.8	3.8	0.5	3.7	0.5
	U (m/s)	0.49	2.15	0.27	0.27	0.72	0.06	0.12	0.59
	0.7	3.4	3.5	1.9	2.2	3.1	1.9	3.7	
	V (m/s)	0.20	1.19	0.01	1.42	1.11	0.38	0.19	0.28
		1.8	0.2	2.0	1.1	2.3	0.1	0.3	3.4
A_4/ϕ_4	TEMP. (°C)	0.37	0.40	0.19	0.27	0.38	0.18	0.35	0.26
		2.0	0.2	0.5	2.9	0.0	2.3	2.6	2.4
	A. P. (hPa)	0.24	0.62	0.60	0.58	0.60	0.19	0.14	0.10
		1.0	1.0	1.1	1.2	1.0	1.2	1.1	1.7
	R. H. (%)	1.71	3.90	5.71	2.14	2.88	1.25	1.19	2.98
		0.3	2.1	2.1	2.1	2.2	2.9	2.4	0.7
	U (m/s)	0.77	1.21	0.32	0.44	0.67	0.24	0.07	0.08
	2.2	2.3	2.8	2.2	2.7	2.6	0.4	1.3	
	V (m/s)	0.84	1.50	0.34	0.85	1.08	0.32	0.09	0.18
		2.8	1.0	0.6	0.4	1.1	1.5	2.5	1.3
EV (%)	TEMP.	62.2	87.7	85.8	88.1	90.5	92.3	93.9	92.4
	A. P.	55.2	75.5	75.9	77.3	70.8	64.5	53.3	56.2
	R. H.	35.8	30.2	58.1	31.2	43.0	40.7	23.8	54.3
	U	47.5	26.7	53.3	28.8	60.7	20.3	93.7	48.0
	V	53.6	29.8	17.8	51.3	56.1	68.4	83.7	25.3

The RH results showed two crucial aspects: the stations located in the north (i.e., San Luis Rio Colorado and Sonoyta) had the lowest RH means, and the stations located in the southeast (Acaponeta, Obispo, and Culiacan) had the highest RH means. Winds showed different behaviors among the sites and had the lowest variances among all the variables

studied. Figures 2–5 show the mean fields, amplitudes, and phases of each weather variable that resulted from the harmonic analysis.

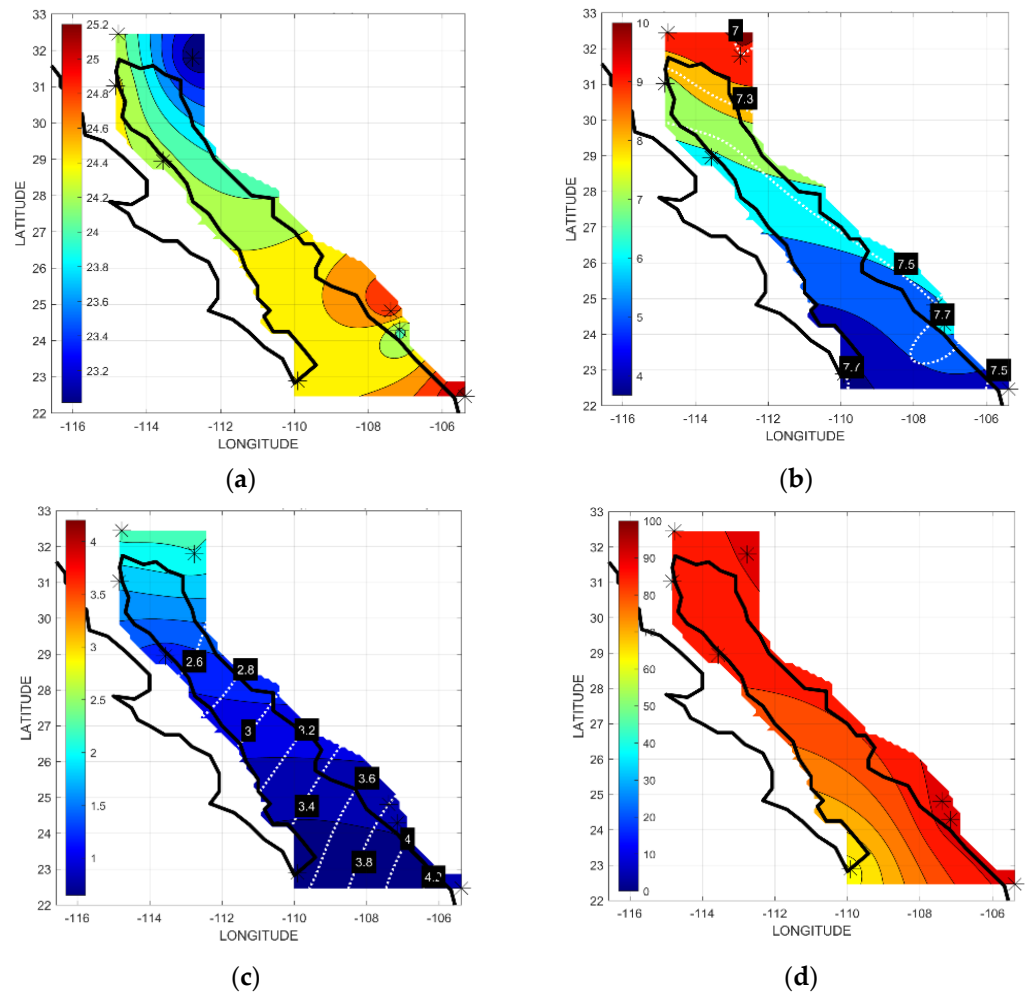


Figure 2. Air temperature harmonic analysis: (a) mean temperature (°C); (b) annual amplitude (°C), phase (months); (c) semiannual amplitude (°C), phase (months); and (d) explained variance (%).

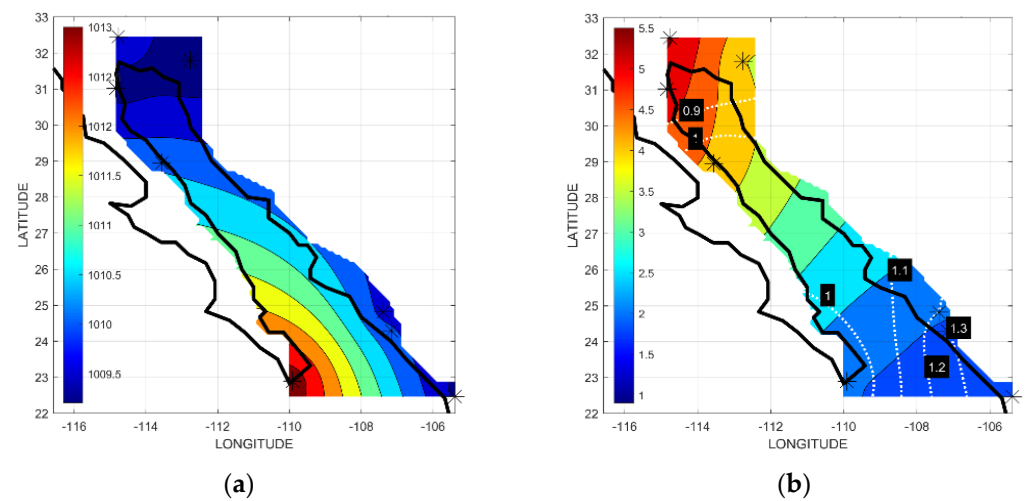


Figure 3. Cont.

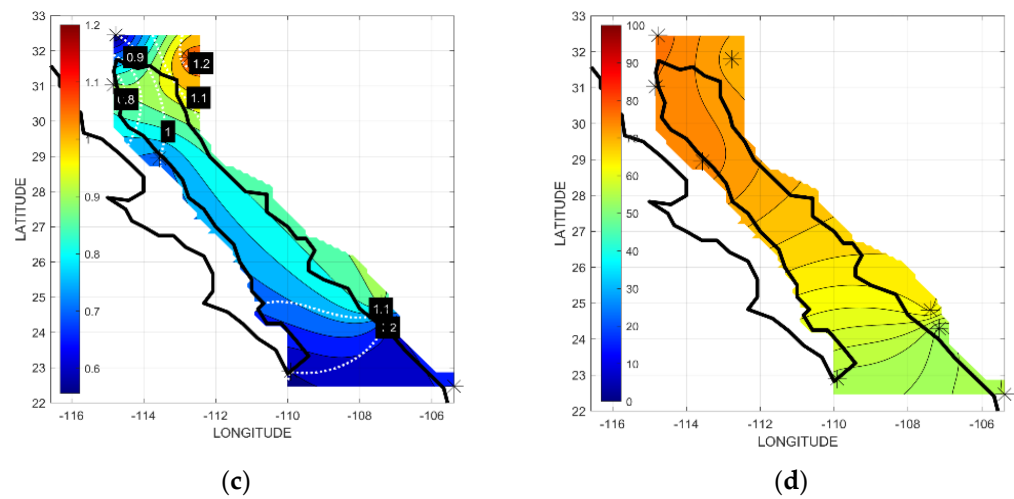


Figure 3. Atmospheric pressure harmonic analysis: (a) mean atmospheric pressure (HPa); (b) annual amplitude (HPa), phase (months); (c) semiannual amplitude (HPa), phase (months); and (d) explained variance (%).

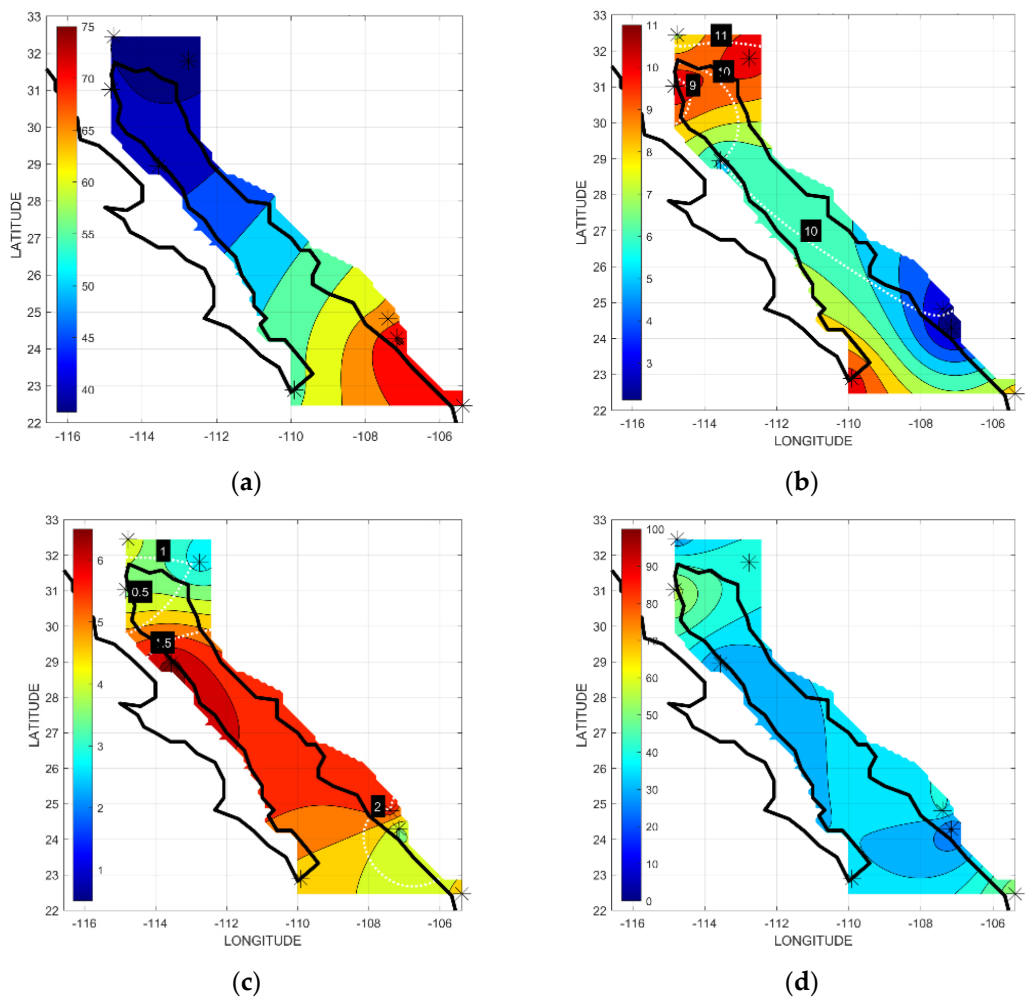


Figure 4. Relative humidity harmonic analysis: (a) mean relative humidity (%); (b) annual amplitude (%), phase (months); (c) semiannual amplitude (%), phase (months); and (d) explained variance (%).

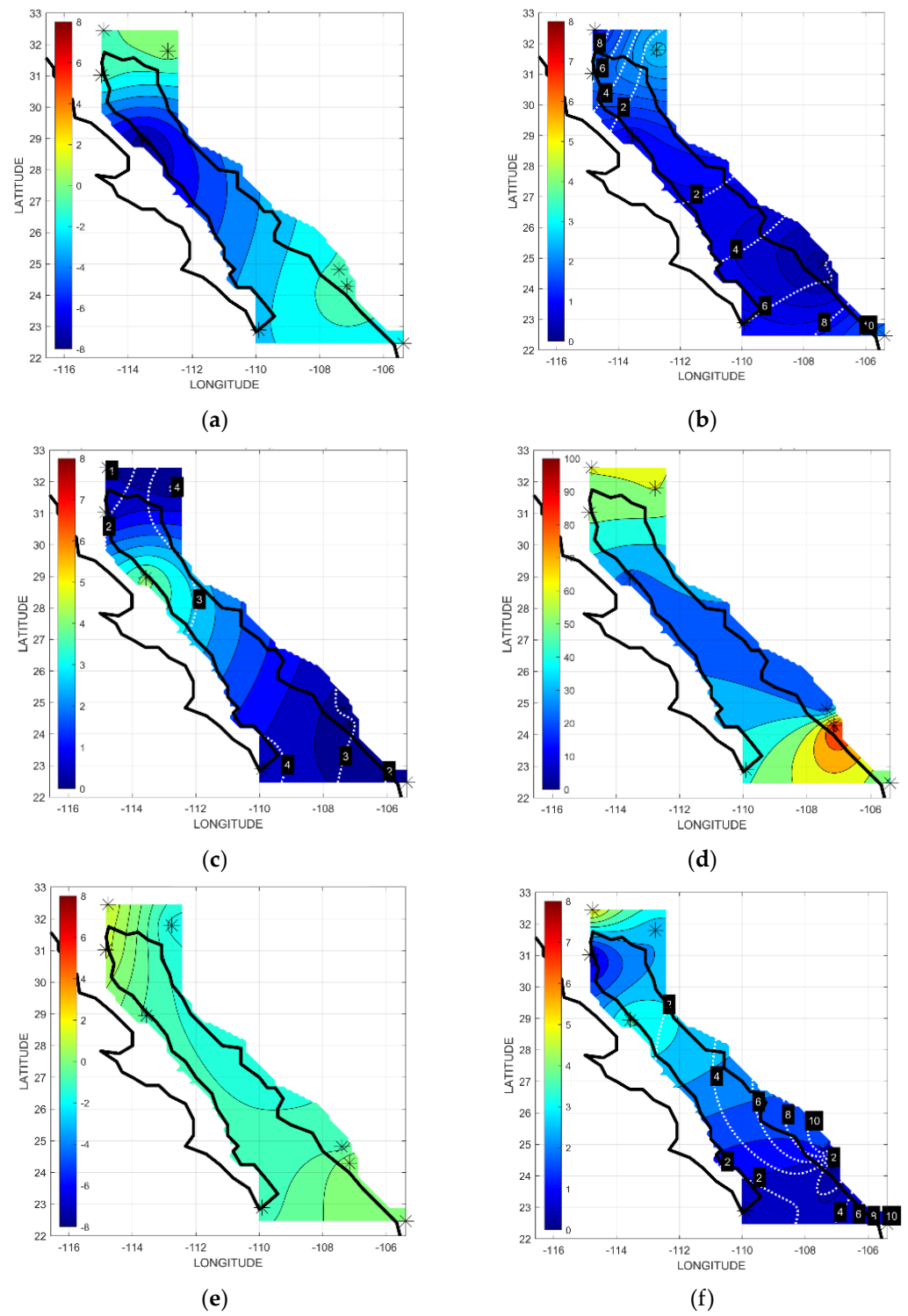


Figure 5. Cont.

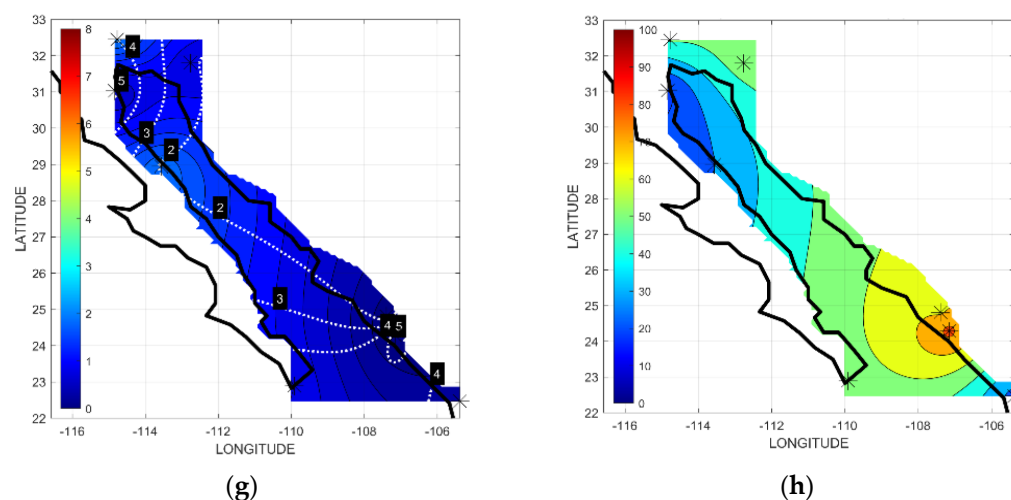


Figure 5. u-wind component harmonic analysis: (a) mean u-wind (m/s); (b) annual amplitude (m/s), phase (months); (c) semiannual amplitude (m/s), phase (months); and (d) explained variance (%); and v-wind component harmonic analysis: (e) mean v-wind (m/s); (f) annual amplitude (m/s), phase (months); (g) semiannual amplitude (m/s), phase (months); and (h) explained variance (%).

Figure 2a displays the mean AT. The highest mean temperatures were in the southeast and decreased progressively northeastward, reaching the lowest means at Sonoyta, close to the Altar Desert. The highest annual amplitude (Figure 2b) was observed in the north (San Luis Rio Colorado and Sonoyta), while the lowest amplitude was in the coastal stations located in the southeast.

The annual amplitude phase (Figure 2b) was reached in early to mid-August, except at Cabo San Lucas and Acaponeta, where it was obtained in late August or early September. The amplitude and semiannual phase (Figure 2c) were homogeneous, except for the stations located in the north, where the amplitude was maximum. The harmonic analysis explained ~90% of the variance, except for Cabo San Lucas, which explained 65% (Figure 2d).

The mean AP field varied from 1009 to 1010 millibars (Figure 3a), except in Cabo San Lucas, where the mean AP was the highest (1013 hPa). The annual amplitude and phase (Figure 3b) were smaller in the mouth of the GoC and increased northwestward. The maxima in the southern and northern parts were in February and January, respectively. The semiannual amplitude and phase (Figure 3c) showed a more homogeneous field, except in Sonoyta. The explained variance (Figure 3d) varied between 70% and 80%, except in Cabo San Lucas, Culiacan, Obispo, and Acaponeta (55%).

Stations in the southeast (i.e., Acaponeta, Obispo, and Culiacan) had the highest RH means (Figure 4a), between 65% and 75%. RH means decreased northward (~40% and 45%), showing that humidity at stations close to the sea was above average. The annual amplitude (Figure 4b) was higher in the northernmost stations, San Felipe, San Luis Rio Colorado, and Sonoyta. The phase indicated that the maximum was reached in November and December. The amplitude and semiannual phase (Figure 4c) were more prominent in the center than in the northern and southern extremes, with explained variances between 35% and 45% (Figure 4d).

The mean wind field characteristics (u and v components; Figure 5) showed that all stations had very similar values (~1 m/s), except the Bahia de Los Angeles station, which showed the highest value. The annual and semiannual amplitudes were homogeneous (Figure 5b,c). The annual phase was reached in several months in the gulf entrance in November, decreasing northwestward and then increasing progressively; the explained variance ranged from 15% in the center of the CG to 85% at the Obispo station.

The mean meridional wind component had values of ~-1 m/s along the coast (Figure 5e), except at the northwestern and southeastern edges, where it showed positive values (~1 m/s). The annual and semiannual amplitudes were homogeneous (Figure 5f,g).

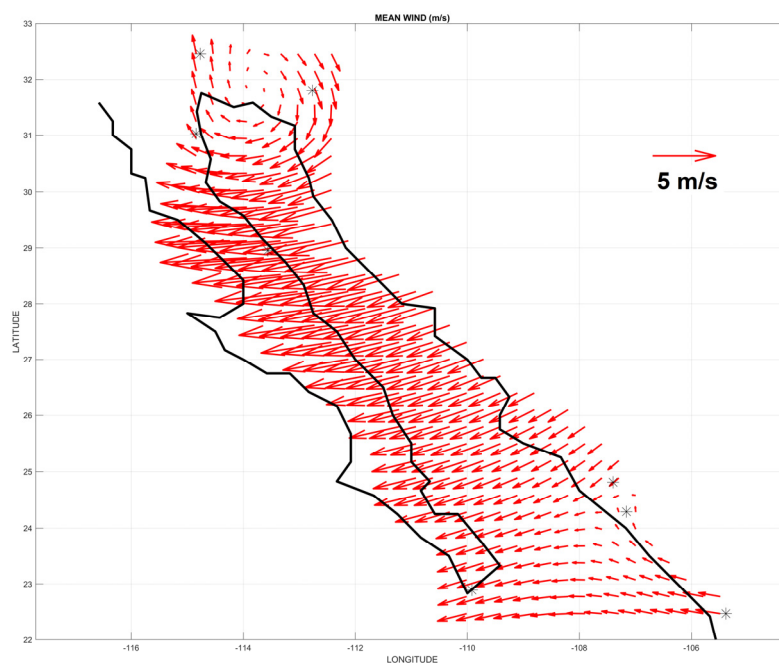
The annual phase was reached in other months, as shown in Figure 5f. The EV in the south was between 50% and 60%, while in the north, it was only between 20% and 30% (Figure 5h).

Figure 6 shows the mean surface wind flow based on eleven years of data (2008–2018), resulting from the mean fields of the zonal (u) and meridional (v) components. The dominant feature was the anticyclonic circulation centered close to the shore on the northern edge of the gulf. The mean wind field indicated that the dominant wind direction was from the east to northeast with maximum intensity in the north–central part of the gulf, which is consistent with Figure 5e.

3.2. Empirical Orthogonal Functions (EOFs)

Figure 7 shows the spatiotemporal values of AT. The first spatial mode (Figure 7a) showed the highest amplitude in the north (San Luis Rio Colorado and Sonoyta) and the lowest amplitude in the south (Cabo San Lucas and Acaponeta, similar to the harmonic analysis results; Figure 2a). In contrast, the second spatial mode (Figure 7b) showed the lowest values ($-5\text{ }^{\circ}\text{C}$) in the north and the highest values ($+5\text{ }^{\circ}\text{C}$) in the south. The first temporal mode (Figure 7c; blue line) showed a robust annual signal, highlighting the winters of 2012 and 2013 and the summers of 2010, 2013, and 2015. The first and second modes explained 95.6% of the variance.

Figure 8a–c show the EOF spatial modes of RH, with the highest amplitude in the north (San Luis Rio Colorado and Sonoyta) and the lowest amplitude in the southeast (Acaponeta, Obispo, and Culiacan). The first temporal mode (Figure 8d) showed the annual signal (blue line), the second the seasonal (red), and the third the intraseasonal (black); the explained variance was $\sim 78\%$.



(a)

Figure 6. Cont.

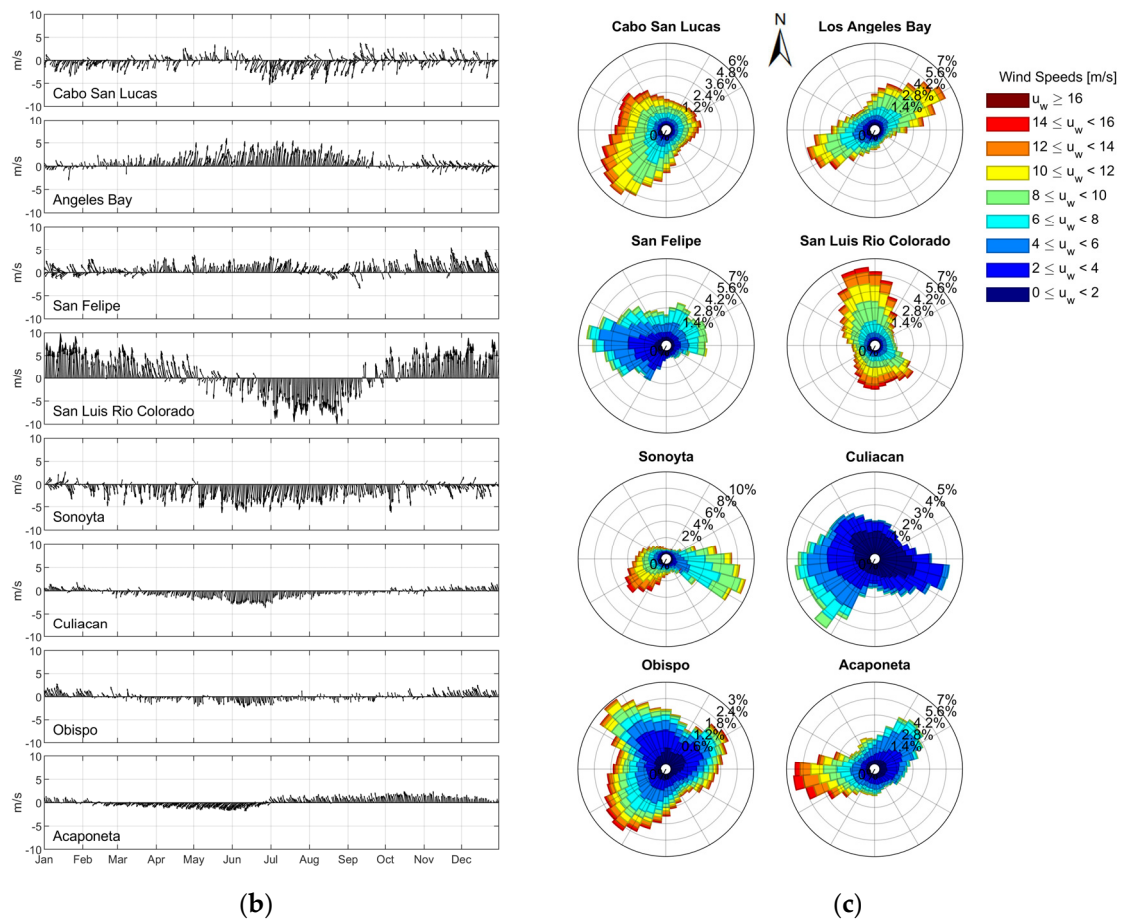


Figure 6. (a) Mean surface wind circulation, (b) canonical year, and (c) diurnal component in the period 2008–2018.

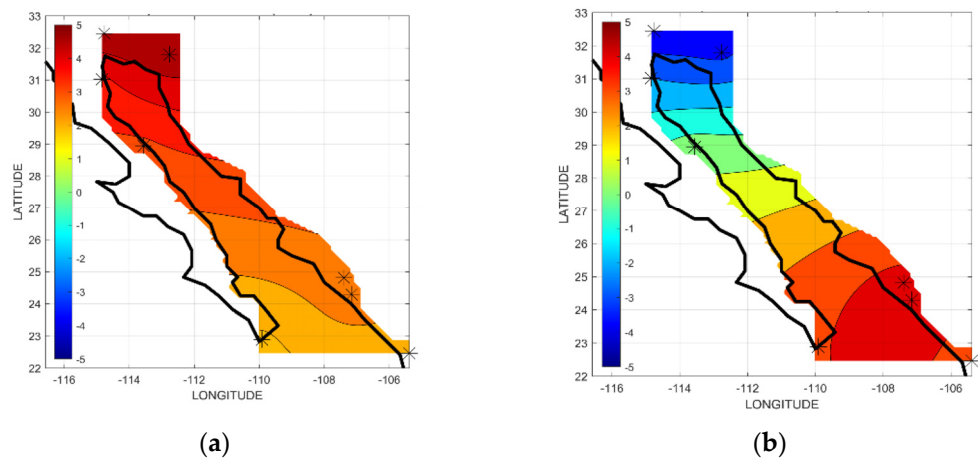
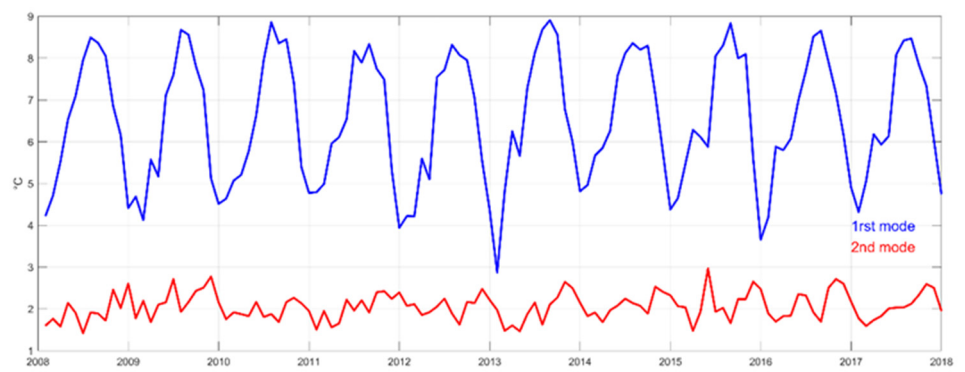
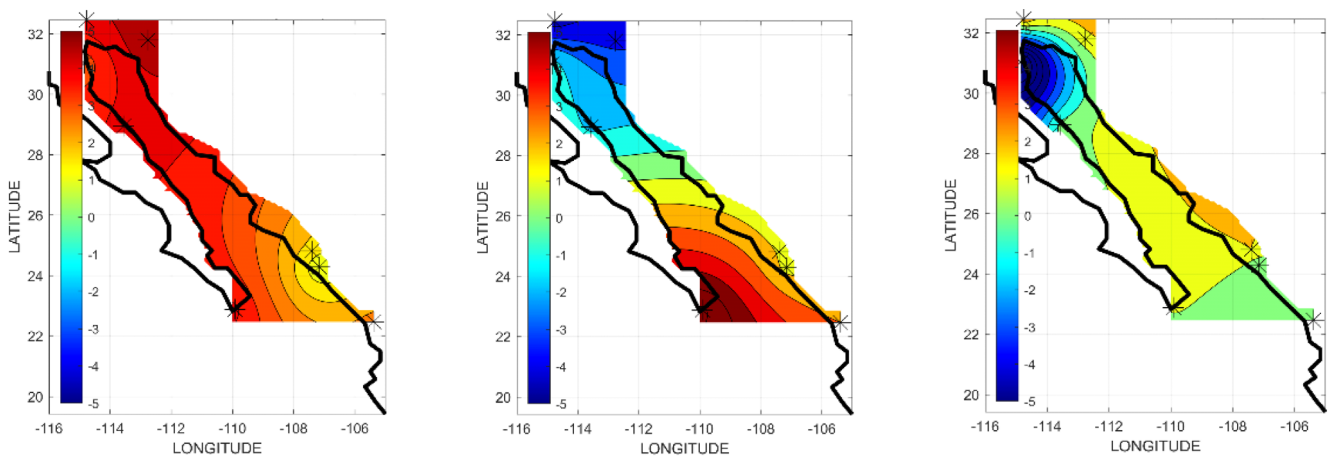


Figure 7. Cont.



(c)

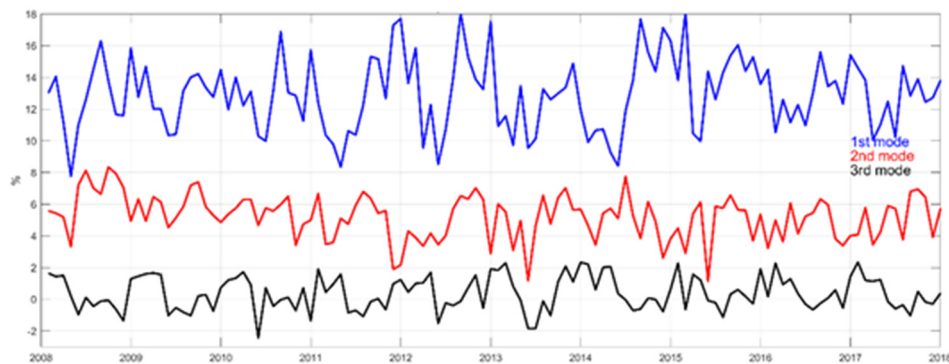
Figure 7. Air temperature EOF: (a) 1st spatial mode (91.5%); (b) 2nd spatial mode (4.1%); (c) temporal modes.



(a)

(b)

(c)



(d)

Figure 8. Relative humidity EOF: (a) 1st spatial mode (48.0%); (b) 2nd spatial mode (19.0%); (c) 3rd spatial mode (10.2%); (d) temporal modes.

The EOF spatial modes of AP (Figure 9) varied little between stations, except for San Felipe and San Luis Rio Colorado, with the highest amplitudes (Figure 9a,b). The first temporal mode in Figure 9c represented a solid annual signal (blue line), and the second (red) represented an intraseasonal signal (Figure 9c); however, the extreme values for 2013–2015 stand out. The EV of the first and second modes was 94.7%.

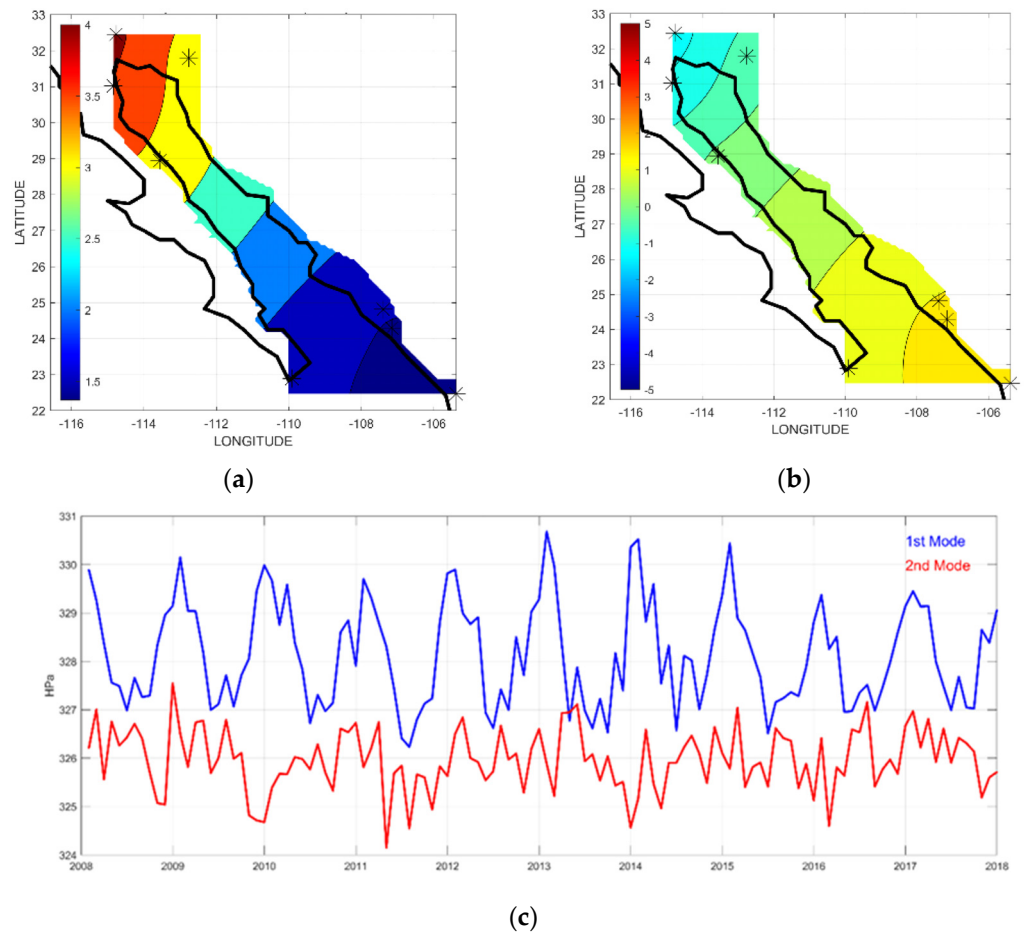


Figure 9. Atmospheric pressure EOF: (a) 1st spatial mode (67.9%); (b) 2nd spatial mode (14.7%); (c) temporal modes.

The wind’s first spatial mode indicated that the maximum amplitude was in the north–central part of the gulf (Figure 10a). In contrast, the second spatial mode reached its maximum amplitude in Sonoyta (Figure 10b). The first temporal mode represented an intraseasonal signal, highlighting the most intense winds in 2012 and 2013, while the second temporal mode highlighted the annual signal. The explained variance was 72.5%.

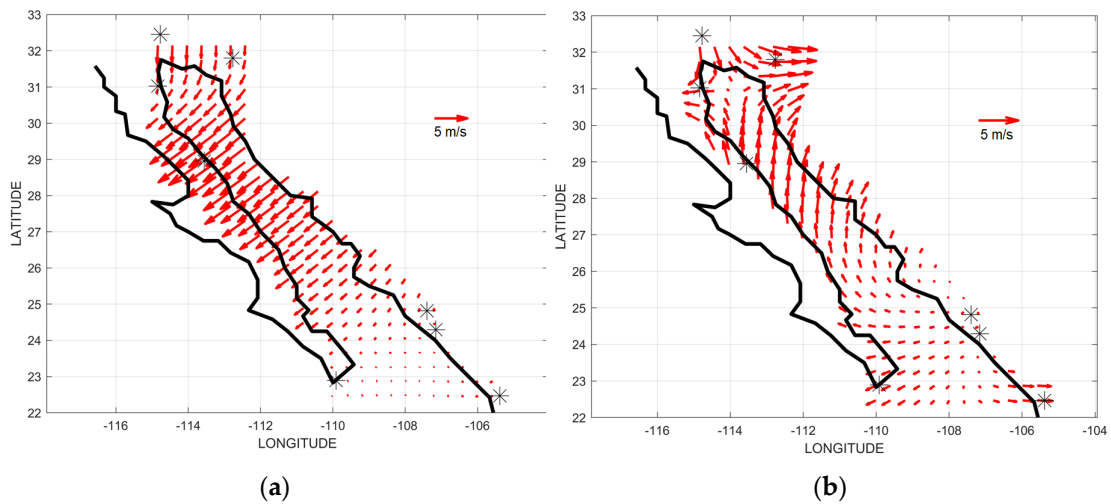


Figure 10. Cont.

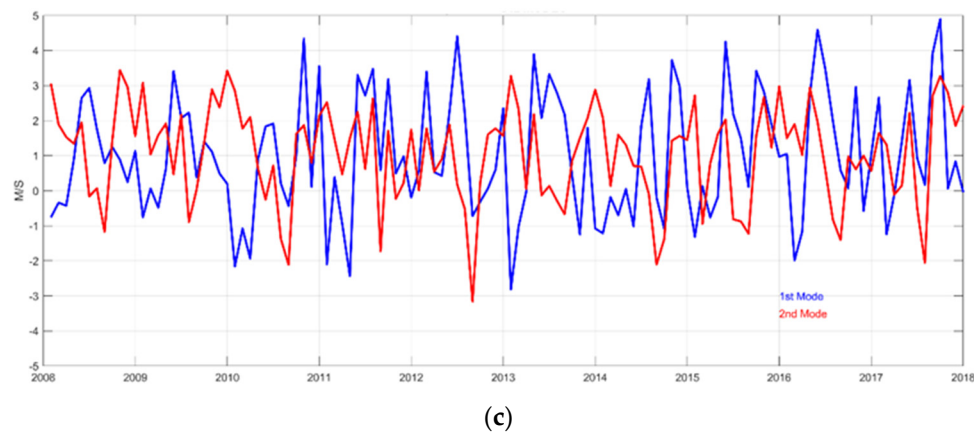


Figure 10. Wind EOF: (a) 1st spatial mode (44.0%); (b) 2nd spatial mode (28.5%); (c) temporal modes.

4. Discussion

4.1. Seasonal Variation

4.1.1. Air Temperature

Figure 11a shows the air temperature spectral analysis of the EOF's temporal modes. It had two prominent peaks representing the annual and semiannual signals, followed by smaller 4-month and 3-month signals. This pattern indicated that seasonal variability was mainly due to factors that recur systematically one or more times per year, such as the sun's apparent northward movement during the boreal summer and the southward movement as the Northern Hemisphere winter approaches [46].

4.1.2. Relative Humidity

Figure 11b shows the spectral analysis of the first three temporal EOF modes. All modes had similar behavior; the most significant signals were the annual and semiannual cycles and, to a lesser extent, fluctuations indicating seasonal and intraseasonal variability.

The seasonal variability in RH was subject to the effects of transient disturbances on different scales. However, perhaps the most important were the winter frontal systems [3] and the summertime Gulf of California moisture surges (i.e., [22–25]). In winter, high RH values result from decreasing air temperature, but sometimes, advection fog is responsible for the air saturation observed in some coastal stations that occur in January or February when warmer air from the sea passes over the seashore's cold surface and heat is transferred from the air to the ground via conduction and turbulent transport [47].

Summer season surges and the low-level jet observed in the southerly flow over the Gulf of California (i.e., [22–25]) were responsible for moisture transport from the Pacific Ocean to the southeastern United States and Mexico. Enhanced warm-season moisture flux into the Gulf of California [48] increased the RH close to saturation at several coastal stations, which occurred because of the abrupt rise in dew point temperature ([49,50]). According to Wu, Schubert, Suarez, and Huang [48], periods of enhanced moisture transport in the gulf are linked to African easterly waves, the Madden Julian Oscillation, and intermediate disturbances from the Caribbean Sea–Western Atlantic Ocean.

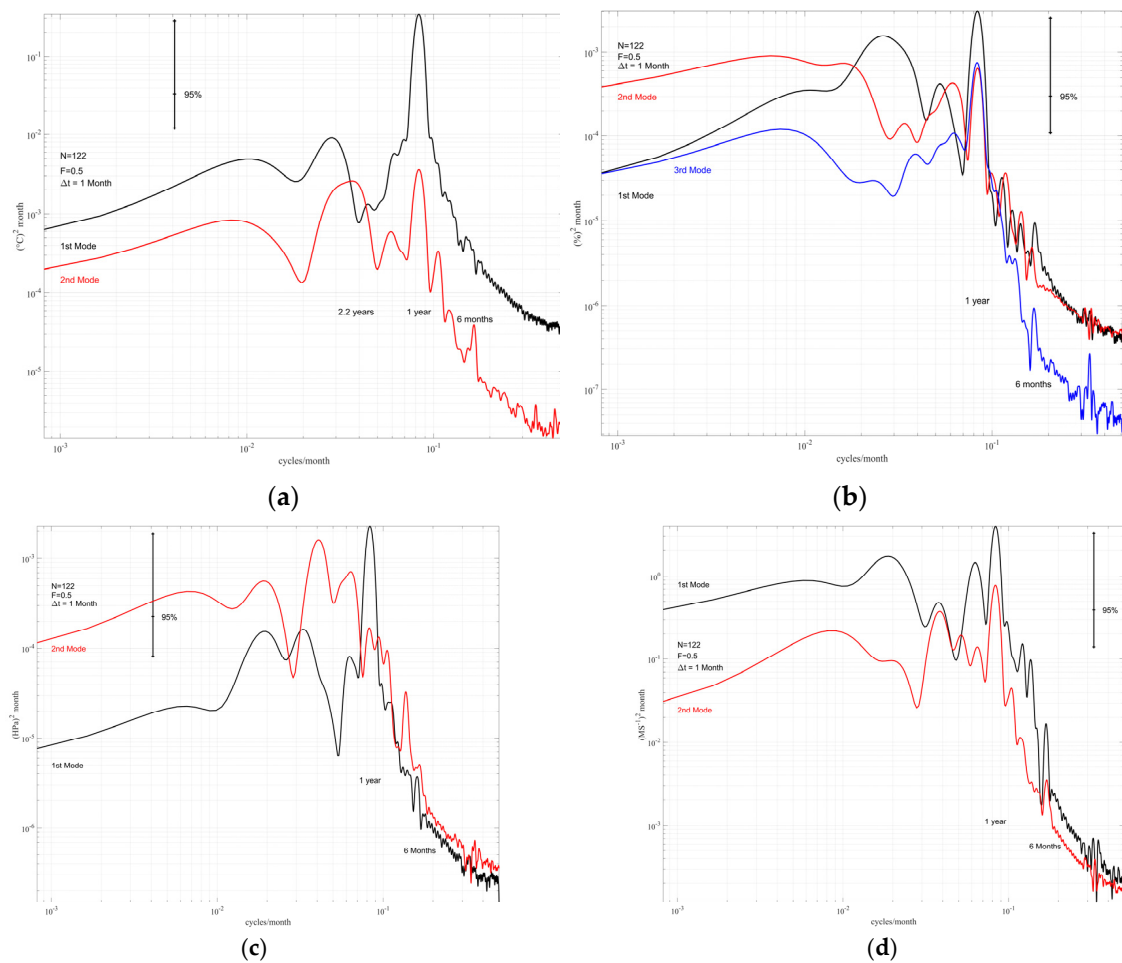


Figure 11. Power spectrum of (a) the air temperature; (b) the relative humidity; (c) the atmospheric pressure; and (d) wind.

4.1.3. Atmospheric Pressure

Figure 11c shows the atmospheric pressure spectral analysis of temporal EOF modes one and two; the annual, semiannual, and seasonal signals are present. They are related to the Pacific high-pressure system since boreal summer (June–August) is located further north than winter (December–February) [46,51,52].

4.1.4. Wind

Figure 11d shows the spectral analysis of the first three temporal EOF modes of wind. All modes had a similar configuration. The most significant signals were the annual and semiannual cycles. To a lesser extent, fluctuations indicated seasonal and intraseasonal variability. The configuration of the flow pattern shown in Figure 10 was consistent with the observed changes from winter to summer during the North American monsoon. The first EOF spatial mode showed a dominant northerly wind component that was characteristic of winter, while the second mode showed a dominant southerly wind component that was characteristic of summer.

A meridional wind circulation pattern (v) that dominated in the lower levels close to the tropical belt was the leading cause of this variability. The Hadley cell dynamics forced this circulation directly from the north–south pressure gradient. The wind across the GoC is usually more intense in winter as a response to the lower amount of solar radiation the ground receives, so the continent is colder than the adjacent oceanic areas [46,51,53].

In general, the wind displayed more significant variability in summer since, from a physical and dynamic point of view, its circulation was much more complex during the

boreal summer than during the winter. The availability of moisture and energy sources throughout the Eastern Tropical Pacific region gives rise to a large set of atmospheric motions, convective activity, and precipitation [46,51–53].

It is important to emphasize that the seasonal signal is an essential feature in climatology. In this study, the seasonal signal was the most important feature. This result was consistent with previous studies in the Gulf of California worldwide; meteorological variables responded mainly to summer–winter warming–cooling, as explained in the following section [42–44].

4.2. Seasonal Synoptic Patterns

4.2.1. Summer

A surface chart analysis (2008–2018) indicated that a synoptic configuration prevailed in the summer and boreal winter and created a large part of the seasonal variability. Figure 12 shows the synoptic configuration that prevails in Mexico. Three meteorological phenomena that prevailed in the mentioned seasons were identified: the convergence zone originated by the Mexican monsoon (A); the advection of tropical maritime air coming from the Pacific Ocean and Gulf of Mexico (B); and the east to west displacement of tropical waves (C), which contributed significantly to moisture transport over the Pacific slope.

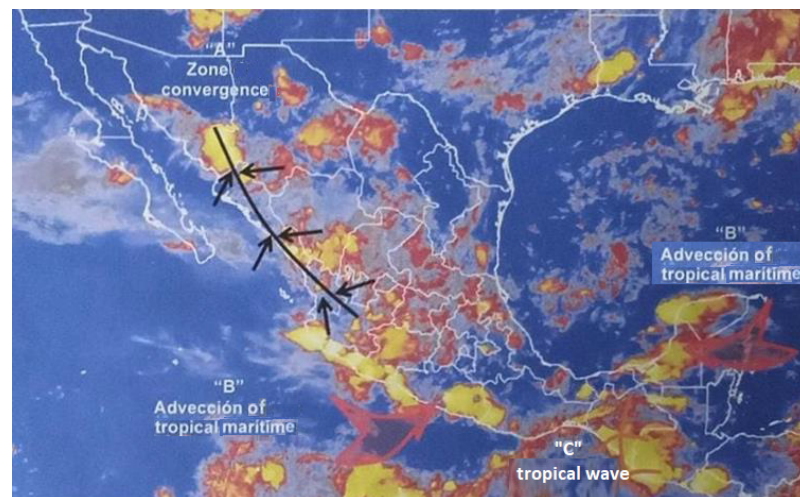


Figure 12. Summer main weather systems.

Tropical cyclones, mesoscale convective systems (MCSs), and precipitation associated with the North American monsoon were the main phenomena that generated the highest amount of moisture in a wide area of northwestern Mexico during summer, with precipitation of more than 200 mm/month, mainly during the afternoons and evenings of July and August [41,54,55]. However, this moisture input did not usually benefit the stations located north of the study area, such as San Felipe, San Luis Rio Colorado, and Sonoyta, which are stations close to the Altar Desert, one of the driest areas in the world.

4.2.2. Winter

Figure 13 shows three weather systems that predominate in a sizeable northwestern part of the country: low-pressure systems (A), the subtropical jet stream (B), and cold fronts (C), which provided humidity and, in most cases, precipitation to the San Felipe, San Luis Rio Colorado, and Sonoyta stations. This explained why the humidity values at these stations were at their highest in winter and not in summer, as expected.



Figure 13. Main weather systems in winter.

As previously discussed, multiple factors affect diurnal and seasonal oscillations, one of which is the existence of the “Sonoran Desert,” which occupies a large territory and, as a desert region, is characterized by low precipitation, high summer temperatures, and wide diurnal and seasonal oscillations [56–58]. In particular, in the northwestern portion of the Sonoran Desert, where the Altar Desert is located, high amplitudes in minimum and maximum temperatures at San Luis Rio Colorado and Sonoyta and minimum RH values are observed to be linked to variations in seasonal surface albedo (i.e., [59]).

4.3. Interannual Variation

Section 3.2 discusses the temporal modes of weather variables (Figures 7–10), which had an intrinsic relationship with the El Niño or La Niña phase, mainly in the summers of 2010, 2013, and 2015, as well as in the winters of 2012 and 2015. However, measuring the relationship between the air temperature and some ENSO indexes was necessary.

Table 3 shows the results of the correlations between the SOI, MEI, and ONI indexes and the air temperature first temporal mode (without the annual signal). The effects of anomalies that originated in the El Niño 3.4 region of the equatorial Pacific Ocean were reflected in the coastal zone of the GoC one year after the anomalies were recorded.

Table 3. Correlations between the SOI, MEI, and ONI indexes vs. air temperature in the first temporal mode using samples of monthly data. Computations were performed allowing a delay from 18 months (second line) to 12 months (last line) between variables. The first column indicates the beginning of air temperature series, while the second column indicates the beginning of SOI, MEI, and ONI indexes. In all cases, n = 98 pairs, and the significance level (lagging n-months) is <0.001.

Years		SOI	MEI	ONI
June 2008	June 2009	−0.47	0.46	0.36
February 2008	June 2009	−0.49	0.49	0.39
March 2008	June 2009	−0.51	0.51	0.41
April 2008	June 2009	−0.52	0.53	0.43
May 2008	June 2009	−0.52	0.54	0.44
June 2008	June 2009	−0.52	0.54	0.44
July 2008	June 2009	−0.51	0.53	0.43

Modified from NOAA [60], NOAA [61], and Quiroz [62].

ENSO events modulate the atmospheric moisture content and air temperatures in the Sonoran Desert (i.e., [63]). However, correlations between ENSOs and winter and

summer temperatures were not linear. The results indicated that the 2009–2010 El Niño episode increased temperatures in the study area during the summer of 2010, but La Niña 2010–2012 caused the lowest temperatures to be recorded in the winter of 2013 in the GoC (Figure 7 [43,44]). These results accounted for the nonlinearity of the relationship between ENSOs and air temperature. For instance, unlike our results, Pavia, Graef, and Reyes [14] found that for mean temperature, cooler conditions are favored during La Niña summers and El Niño winters regardless of the PDO phase, and a high PDO favors warmer conditions during El Niño summers. This situation is complicated when moisture (i.e., rainfall) and ENSOs are correlated [64,65]. However, the connection between below-average winter precipitation and La Niña events is much stronger than that between above-average winter precipitation and El Niño events [66]. Zolotokrylin, Titkova, and Brito-Castillo [63] mentioned that wet conditions in the Sonoran Desert during May–September increase shifts from El Niño to La Niña events. Many studies have attempted to establish a relationship between ENSO phases and rainfall in northwestern Mexico. For instance, Vega-Camarena, Brito-Castillo, Pineda-Martínez, and Farfán [64] and Vega-Camarena, Brito-Castillo, Farfán, Gochis, Pineda-Martínez, and Díaz [65] found that rainfall production in the Altiplano (Mexican Plateau), located to the south of the monsoon region, depends not only on the ENSO phase but also on the phase combination between PDO and AMO. They concluded that above-average rainfall occurs from the transition from El Niño to La Niña or La Niña to El Niño events. Perhaps this is the reason why several authors failed to find a consistent relationship between ENSO and summer rains in northwestern Mexico (i.e., [67–69]). Vega-Camarena, Brito-Castillo, Farfán, Gochis, Pineda-Martínez, and Díaz [65] and Seager, Kushnir, Herweijer, Naik, and Velez [69] reported that La Niña conditions, in combination with the cold phase of the PDO and warm phase of the AMO, are associated with weaker-than-normal moisture flows from the tropical southeastern to northern Mexico regions. Such combinations result in intense droughts and reductions in the number of hurricanes in the Pacific [70].

In addition, Johnson and Delworth [71] highlight the significant role of the GoC in the monsoon region of North America. They emphasize that the GoC plays a substantial role in supplying moisture at lower atmospheric levels, which greatly influences precipitation patterns in this region. As a consequence of this moisture supply, the North American monsoon region experiences significantly higher precipitation levels than the surrounding areas. This increase in precipitation has profound implications for the spatial and temporal distribution of rainfall. The presence of the GoC results in a clear precipitation gradient across the region, with areas closer to the GoC experiencing more abundant precipitation. Furthermore, the timing and duration of precipitation are also influenced by the presence of the GoC. Moisture from the GoC interacts with prevailing winds and atmospheric conditions, resulting in the development of localized convective systems and increased precipitation during the monsoon season [71].

5. Conclusions

Ground observations from automatic weather stations were provided by CNA. The data were used to construct a climatology of the GoC coastal zone.

The highest AT averages were found in Acaponeta and Culiacan in the southeast. At the northern stations (San Luis Rio Colorado and Sonoyta), a greater amplitude in the diurnal oscillation of AT could be attributed to the seasonal variations in surface albedo in the Altar Desert, displaying extreme values of the minimum and maximum temperatures.

The RH at the GoC entrance (Acaponeta, Culiacan, and Obispo) maintained a high percentage (67% and 76%) throughout the year, reaching 100% on several days, which occurred in Obispo. Moisture increased in summer, mainly favored by the low-level jet over the GoC and the occurrence of gulf surges during the Mexican monsoon. Other transient disturbances also contributed to moisture increases in the area, such as tropical storms, mesoscale convective systems, and easterly waves. In comparison, San Luis Rio Colorado and Sonoyta were the driest stations. The RH there reached between 38% and 40% in

winter, and this characteristic increased with the arrival of winter systems (i.e., cold fronts, troughs, and low pressure) and the decrease in air temperature.

The AP showed little change, except at the northern stations (San Luis Rio Colorado and Sonoyta), where the most significant amplitudes were observed, likely because these stations are farther from the coastal zone than other stations and are more sensitive to the north–south movement, or vice versa, of the Pacific high-pressure system, for which the sea acts as a regulator.

In the study area, the annual signal predominated, followed by those of greater frequency (seasonal and intraseasonal) and, to a lesser extent, an interannual signal associated with the ENSO phenomenon in its warm and cold phases.

The variables analyzed differed on the coasts of the GoC; the seasonal profiles showed that in the eastern part, they were homogeneous (the variables did not change much), and on the west coast, the profiles were heterogeneous (the values varied significantly between each meteorological station), which was attributed to local weather systems.

Although it was found that the summer and winter seasons were most defined by the dominant synoptic configuration in the area, the spectral analysis showed that low frequencies presented the highest energy, indicating that the most significant variability is due to seasonal and intraseasonal changes.

On the interannual scale, events associated with El Niño were detected, which caused an increase in the air temperature in summer. During La Niña, the coldest temperatures were recorded in winter, mainly in 2013, indicating that ENSO is associated with the anomalies of the weather characteristics studied in this work.

Author Contributions: Conceptualization, E.P.-H., J.M.M.-A. and D.A.-C.; methodology, E.P.-H., J.M.M.-A., S.J.-C., L.B.-C., L.C. and D.A.-C.; software, E.P.-H., S.J.-C. and D.A.-C.; validation, E.P.-H., J.M.M.-A., L.B.-C., L.C. and D.A.-C.; formal analysis, E.P.-H., S.J.-C., L.B.-C. and D.A.-C.; investigation, E.P.-H., J.M.M.-A., S.J.-C., L.B.-C., L.C. and D.A.-C.; resources, E.P.-H.; data curation, E.P.-H., S.J.-C., L.C. and D.A.-C.; writing—original draft preparation, E.P.-H., J.M.M.-A., S.J.-C., L.B.-C., L.C. and D.A.-C.; writing—review and editing, E.P.-H., S.J.-C., L.B.-C. and D.A.-C.; visualization, E.P.-H., L.B.-C., L.C. and D.A.-C.; supervision, E.P.-H. and D.A.-C.; project administration, E.P.-H.; funding acquisition, E.P.-H. All authors have read and agreed to the published version of the manuscript.

Funding: Basic Science projects, CONACYT: 3209-T9207; 000000000104884 and 44870F.

Data Availability Statement: Not applicable.

Acknowledgments: Basic Science projects, CONACYT: 3209-T9207; 000000000104884 and 44870F, the experiments comply with the current laws of México, David González and Camila González, English revision. The authors are grateful to Julio Egrén Félix Domínguez from CIBNOR Spatial Modeling and Remote Sensing Laboratory for technical support in obtaining automatic weather station data.

Conflicts of Interest: The authors declare no conflict of interest.

Appendix A

The relative error in each mesh point is the difference between the original data and the interpolation divided by that original data ($x - \frac{x_i}{x}$), which is related to the correlation radius (50) in the mapping (Figure A1).

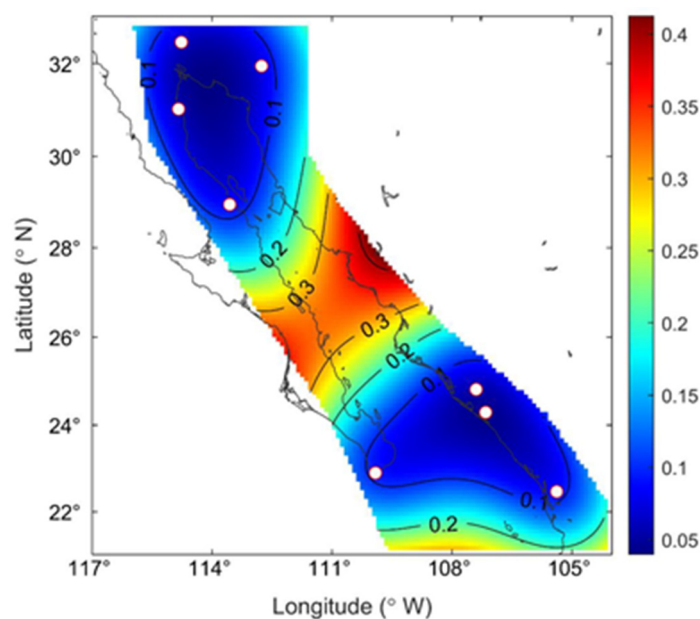


Figure A1. Interpolation relative error.

References

- Farfán, L.M.; Barrett, B.S.; Raga, G.B.; Delgado, J.J. Characteristics of mesoscale convection over northwestern Mexico, the Gulf of California, and Baja California Peninsula. *Int. J. Climatol.* **2021**, *41*, E1062–E1084. [\[CrossRef\]](#)
- Gochis, D.J.; Watts, C.J.; Garatuza-Payan, J.; Cesar-Rodriguez, J. Spatial and Temporal Patterns of Precipitation Intensity as Observed by the NAME Event Rain Gauge Network from 2002 to 2004. *J. Clim.* **2007**, *20*, 1734–1750. [\[CrossRef\]](#)
- Nesbitt, S.W.; Gochis, D.J.; Lang, T.J. The Diurnal Cycle of Clouds and Precipitation along the Sierra Madre Occidental Observed during NAME-2004: Implications for Warm Season Precipitation Estimation in Complex Terrain. *J. Hydrometeorol.* **2008**, *9*, 728–743. [\[CrossRef\]](#)
- Rowe, A.K.; Rutledge, S.A.; Lang, T.J.; Ciesielski, P.E.; Saleeby, S.M. Elevation-Dependent Trends in Precipitation Observed during NAME. *Mon. Weather Rev.* **2008**, *136*, 4962–4979. [\[CrossRef\]](#)
- Arriaga-Ramírez, S.; Cavazos, T. Regional trends of daily precipitation indices in northwest Mexico and southwest United States. *J. Geophys. Res. Atmos.* **2010**, *115*, D14111. [\[CrossRef\]](#)
- Brito-Castillo, L.; Díaz-Castro, S.; Salinas-Zavala, C.A.; Douglas, A.V. Reconstruction of long-term winter streamflow in the Gulf of California continental watershed. *J. Hydrol.* **2003**, *278*, 39–50. [\[CrossRef\]](#)
- Castillo, M.; Muñoz-Salinas, E.; Sanderson, D.C.W.; Cresswell, A. Landscape evolution of Punta Arena sand spit (SE Baja California Peninsula, NW Mexico): Implications of ENSO on landscape erosion rates. *Catena* **2020**, *193*, 104601. [\[CrossRef\]](#)
- Cavazos, T.; Luna-Niño, R.; Cerezo-Mota, R.; Fuentes-Franco, R.; Méndez, M.; Pineda Martínez, L.F.; Valenzuela, E. Climatic trends and regional climate models intercomparison over the CORDEX-CAM (Central America, Caribbean, and Mexico) domain. *Int. J. Climatol.* **2020**, *40*, 1396–1420. [\[CrossRef\]](#)
- Conde Alvarez, A.C. Cambio y Variabilidad Climáticos. Dos Estudios de Caso en México. Ph.D. Thesis, Universidad Nacional Autónoma de México, Distrito Federal, Mexico, 2003.
- Del-Toro-Guerrero, F.J.; Kretzschmar, T. Precipitation-temperature variability and drought episodes in northwest Baja California, México. *J. Hydrol. Reg. Stud.* **2020**, *27*, 100653. [\[CrossRef\]](#)
- Diaz, S.C.; Salinas-Zavala, C.A.; Arriaga, L. An interannual climatological aridity series for the Sierra de La Laguna, B.C.S. Mexico. *Mt. Res. Dev.* **1994**, *14*, 137–146. [\[CrossRef\]](#)
- Dominguez, C.; Jaramillo, A.; Cuéllar, P. Are the socioeconomic impacts associated with tropical cyclones in Mexico exacerbated by local vulnerability and ENSO conditions? *Int. J. Climatol.* **2021**, *41*, E3307–E3324. [\[CrossRef\]](#)
- Morales-Acuña, E.; Torres, C.; Delgadillo-Hinojosa, F.; Linero-Cueto, J.; Santamaría-Del-Ángel, E.; Castro, R. The Baja California Peninsula, a Significant Source of Dust in Northwest Mexico. *Atmosphere* **2019**, *10*, 582. [\[CrossRef\]](#)
- Pavia, E.G.; Graef, F.; Reyes, J. PDO–ENSO Effects in the Climate of Mexico. *J. Clim.* **2006**, *19*, 6433–6438. [\[CrossRef\]](#)
- Brito-Castillo, L.; Douglas, A.V.; Leyva-Contreras, A.; Lluch-Belda, D. The effect of large-scale circulation on precipitation and streamflow in the Gulf of California continental watershed. *Int. J. Climatol.* **2003**, *23*, 751–768. [\[CrossRef\]](#)
- Higgins, R.W.; Silva, V.B.S.; Shi, W.; Larson, J. Relationships between climate variability and fluctuations in daily precipitation over the United States. *J. Clim.* **2007**, *20*, 3561–3579. [\[CrossRef\]](#)
- Mantua, N.J.; Hare, S.R. The Pacific Decadal Oscillation. *J. Oceanogr.* **2002**, *58*, 35–44. [\[CrossRef\]](#)
- Torres, V.M.; Thorncroft, C.D. Interdecadal Variability of Easterly Waves Over the Tropical Northeastern Pacific. *Geophys. Res. Lett.* **2022**, *49*, e2022GL099090. [\[CrossRef\]](#)

19. Wright, K.T.; Johnson, K.R.; Bhattacharya, T.; Marks, G.S.; McGee, D.; Elsbury, D.; Peings, Y.; Lacaille-Muzquiz, J.-L.; Lum, G.; Beramendi-Orosco, L.; et al. Precipitation in Northeast Mexico Primarily Controlled by the Relative Warming of Atlantic SSTs. *Geophys. Res. Lett.* **2022**, *49*, e2022GL098186. [[CrossRef](#)]
20. Brito-Castillo, L.; Alcocer-Vázquez, M.D.; Félix-Domínguez, J.E. Características de los vientos superficiales en Sonora: Información relevante para el aprovechamiento del recurso y prevención de desastres. *Quehacer Científico En Chiapas* **2019**, *14*, 33–45.
21. Bordoni, S.; Ciesielski, P.E.; Johnson, R.H.; McNoldy, B.D.; Stevens, B. The low-level circulation of the North American Monsoon as revealed by QuikSCAT. *Geophys. Res. Lett.* **2004**, *31*, L10109. [[CrossRef](#)]
22. Bordoni, S.; Stevens, B. Principal Component Analysis of the Summertime Winds over the Gulf of California: A Gulf Surge Index. *Mon. Weather Rev.* **2006**, *134*, 3395–3414. [[CrossRef](#)]
23. Douglas, M.W. The Summertime Low-Level Jet over the Gulf of California. *Mon. Weather Rev.* **1995**, *123*, 2334–2347. [[CrossRef](#)]
24. Stensrud, D.J.; Gall, R.L.; Nordquist, M.K. Surges over the Gulf of California during the Mexican Monsoon. *Mon. Weather Rev.* **1997**, *125*, 417–437. [[CrossRef](#)]
25. Douglas, M.W.; Valdez-Manzanilla, A.; Garcia Cueto, R. Diurnal Variation and Horizontal Extent of the Low-Level Jet over the Northern Gulf of California. *Mon. Weather Rev.* **1998**, *126*, 2017–2025. [[CrossRef](#)]
26. Ciesielski, P.E.; Johnson, R.H. Diurnal Cycle of Surface Flows during 2004 NAME and Comparison to Model Reanalysis. *J. Clim.* **2008**, *21*, 3890–3913. [[CrossRef](#)]
27. IPCC. *Climate Change 2021: The Physical Science Basis*; Masson-Delmotte, V., Zhai, P., Pirani, A., Connors, S.L., Péan, C., Berger, S., Caud, N., Chen, Y., Goldfarb, L., Gomis, M., Eds.; Cambridge University Press: Cambridge, UK; New York, NY, USA, 2021; Volume 2, p. 2391.
28. Ripple, W.J.; Wolf, C.; Gregg, J.W.; Levin, K.; Rockström, J.; Newsome, T.M.; Betts, M.G.; Huq, S.; Law, B.E.; Kemp, L.; et al. World Scientists' Warning of a Climate Emergency 2022. *BioScience* **2022**, *72*, 1149–1155. [[CrossRef](#)]
29. Wang, S.; Toumi, R. Recent tropical cyclone changes inferred from ocean surface temperature cold wakes. *Sci. Rep.* **2021**, *11*, 22269. [[CrossRef](#)]
30. Magaña Rueda, V.O. *Los Impactos de el Niño en México*; Universidad Nacional Autónoma de México: Mexico City, Mexico, 2001.
31. García, E. *Modificaciones al Sistema de Clasificación Climática de Köppen; (Para Adaptarlo a las Condiciones de la República Mexicana)*; Universidad Nacional Autónoma de México: Mexico City, Mexico, 1987.
32. Douglas, M.W.; Maddox, R.A.; Howard, K.; Reyes, S. The Mexican Monsoon. *J. Clim.* **1993**, *6*, 1665–1677. [[CrossRef](#)]
33. Barlow, M.; Nigam, S.; Berbery, E.H. Evolution of the North American Monsoon System. *J. Clim.* **1998**, *11*, 2238–2257. [[CrossRef](#)]
34. Gochis, D.J.; Brito-Castillo, L.; Shuttleworth, W.J. Hydroclimatology of the North American Monsoon region in northwest Mexico. *J. Hydrol.* **2006**, *316*, 53–70. [[CrossRef](#)]
35. Verduzco, V.S.; Garatuza-Payán, J.; Yépez, E.A.; Watts, C.J.; Rodríguez, J.C.; Robles-Morua, A.; Vivoni, E.R. Variations of net ecosystem production due to seasonal precipitation differences in a tropical dry forest of northwest Mexico. *J. Geophys. Res. Biogeosci.* **2015**, *120*, 2081–2094. [[CrossRef](#)]
36. Brito-Castillo, L.; Farfán, L.M.; Antemate-Velasco, G.J. Effect of the Trans-Volcanic Axis on meridional propagation of summer precipitation in western Mexico. *Int. J. Climatol.* **2022**, *42*, 9304–9318. [[CrossRef](#)]
37. Wang, C.; Fiedler, P.C. ENSO variability and the eastern tropical Pacific: A review. *Prog. Oceanogr.* **2006**, *69*, 239–266. [[CrossRef](#)]
38. Bernal, G.; Ripa, P.; Herguera, J.C. Oceanographic and climatic variability in the lower Gulf of California: Links with the tropics and North Pacific. *Cienc. Mar.* **2001**, *27*, 595–617. [[CrossRef](#)]
39. Dunkerley, D. The Ecohydrology of Desert Environments: What Makes it Distinctive? In *Encyclopedia of the World's Biomes*; Goldstein, M.L., DellaSala, D.A., Eds.; Elsevier: Oxford, UK, 2020; pp. 23–35.
40. Schmidt, R.H. The arid zones of Mexico: Climatic extremes and conceptualization of the Sonoran Desert. *J. Arid Environ.* **1989**, *16*, 241–256. [[CrossRef](#)]
41. Reyes, S.; Douglas, M.W.; Maddox, R.A. El monzón del suroeste de Norteamérica (TRAVASON/SWAMP). *Atmósfera* **1994**, *7*, 117–137.
42. Ripa, P. Least squares data fitting. *Cienc. Mar.* **2002**, *28*, 79–105. [[CrossRef](#)]
43. Cepeda-Morales, J.; Gaxiola-Castro, G.; Beier, E.; Godínez, V.M. The mechanisms involved in defining the northern boundary of the shallow oxygen minimum zone in the eastern tropical Pacific Ocean off Mexico. *Deep Sea Res. Part I Oceanogr. Res. Pap.* **2013**, *76*, 1–12. [[CrossRef](#)]
44. Olascoaga, M.J.; Beron-Vera, F.J.; Miron, P.; Triñanes, J.; Putman, N.F.; Lumpkin, R.; Goni, G.J. Observation and quantification of inertial effects on the drift of floating objects at the ocean surface. *Phys. Fluids* **2020**, *32*, 026601. [[CrossRef](#)]
45. Oliver, M.A.; Webster, R. Kriging: A method of interpolation for geographical information systems. *Int. J. Geogr. Inf. Syst.* **1990**, *4*, 313–332. [[CrossRef](#)]
46. Amador, J.A.; Alfaro, E.J.; Lizano, O.G.; Magaña, V.O. Atmospheric forcing of the eastern tropical Pacific: A review. *Prog. Oceanogr.* **2006**, *69*, 101–142. [[CrossRef](#)]
47. Neiburger, M.; Edinger, J.G.; Bonner, W.D. *Understanding Our Atmospheric Environment*; W.H. Freeman: New York, NY, USA, 1973.
48. Wu, M.-L.C.; Schubert, S.D.; Suarez, M.J.; Huang, N.E. An Analysis of Moisture Fluxes into the Gulf of California. *J. Clim.* **2009**, *22*, 2216–2239. [[CrossRef](#)]
49. Hales, J.E. Surges of Maritime Tropical Air Northward Over the Gulf of California. *Mon. Weather Rev.* **1972**, *100*, 298–306. [[CrossRef](#)]

50. Brenner, I.S. A Surge of Maritime Tropical Air—Gulf of California to the Southwestern United States. *Mon. Weather Rev.* **1974**, *102*, 375–389. [[CrossRef](#)]
51. Amador, J.A.; Arce-Fernández, D. WWLLN Hot and Cold-Spots of Lightning Activity and Their Relation to Climate in an Extended Central America Region 2012–2020. *Atmosphere* **2022**, *13*, 76. [[CrossRef](#)]
52. Willeit, M.; Ganopolski, A.; Robinson, A.; Edwards, N.R. The Earth system model CLIMBER-X v1.0—Part 1: Climate model description and validation. *Geosci. Model Dev.* **2022**, *15*, 5905–5948. [[CrossRef](#)]
53. Lin, J.; Qian, T.; Bechtold, P.; Grell, G.; Zhang, G.J.; Zhu, P.; Freitas, S.R.; Barnes, H.; Han, J. Atmospheric Convection. *Atmosphere-Ocean* **2022**, *60*, 422–476. [[CrossRef](#)]
54. Ramos-Pérez, O.; Adams, D.K.; Ochoa-Moya, C.A.; Quintanar, A.I. A Climatology of Mesoscale Convective Systems in Northwest Mexico during the North American Monsoon. *Atmosphere* **2022**, *13*, 665. [[CrossRef](#)]
55. Clapp, C.E.; Smith, J.B.; Bedka, K.M.; Anderson, J.G. Identifying Outflow Regions of North American Monsoon Anticyclone-Mediated Meridional Transport of Convectively Influenced Air Masses in the Lower Stratosphere. *J. Geophys. Res. Atmos.* **2021**, *126*, e2021JD034644. [[CrossRef](#)]
56. Colorado-Ruiz, G.; Cavazos, T. Trends of daily extreme and non-extreme rainfall indices and intercomparison with different gridded data sets over Mexico and the southern United States. *Int. J. Climatol.* **2021**, *41*, 5406–5430. [[CrossRef](#)]
57. Cortés-Ramos, J.; Farfán, L.M.; Brito-Castillo, L. Extreme freezing in the Sonoran Desert, Mexico: Intense and short-duration events. *Int. J. Climatol.* **2021**, *41*, 4339–4358. [[CrossRef](#)]
58. Jáuregui, E.; Cruz Navarro, F. Algunos aspectos del clima de Sonora y Baja California: Equipatas y surgencias de humedad. *Investig. Geográficas* **1980**, 143–180. [[CrossRef](#)]
59. Gaxiola-Morales, M.G.; Brito-Castillo, L. Análisis de los factores de radiación-evapotranspiración en el Desierto Sonorense. *Biotecnía* **2019**, *21*, 137–144. [[CrossRef](#)]
60. NOAA. Multivariate ENSO Index Version 2 (MEI.v2). Available online: <https://psl.noaa.gov/enso/mei/> (accessed on 23 February 2022).
61. NOAA. Southern Oscillation Index (SOI). Available online: <https://www.ncdc.noaa.gov/teleconnections/enso/indicators/soi/> (accessed on 23 February 2022).
62. Quiroz, M. *Anexo del Informe Técnico: Elaboración de un Boletín con Información Hidroclimática de los Mares de México*; INAPESCA: Ciudad de México, Mexico, 2011; p. 27.
63. Zolotokrylin, A.N.; Titkova, T.B.; Brito-Castillo, L. Wet and dry patterns associated with ENSO events in the Sonoran Desert from, 2000–2015. *J. Arid Environ.* **2016**, *134*, 21–32. [[CrossRef](#)]
64. Vega-Camarena, J.P.; Brito-Castillo, L.; Pineda-Martínez, L.F.; Farfán, L.M. ENSO Impact on Summer Precipitation and Moisture Fluxes over the Mexican Altiplano. *J. Mar. Sci. Eng.* **2023**, *11*, 1083. [[CrossRef](#)]
65. Vega-Camarena, J.P.; Brito-Castillo, L.; Farfán, L.M.; Gochis, D.J.; Pineda-Martínez, L.F.; Díaz, S.C. Ocean–atmosphere conditions related to severe and persistent droughts in the Mexican Altiplano. *Int. J. Climatol.* **2018**, *38*, 853–866. [[CrossRef](#)]
66. Rasmusson, E.M.; Wallace, J.M. Meteorological Aspects of the El Niño/Southern Oscillation. *Science* **1983**, *222*, 1195–1202. [[CrossRef](#)]
67. Castro, L.C.; McKee, T.B.; Pielke, R.A. The Relationship of the North American Monsoon to Tropical and North Pacific Sea Surface Temperatures as Revealed by Observational Analyses. *J. Clim.* **2001**, *14*, 4449–4473. [[CrossRef](#)]
68. Reyes, S.; Mejía-Trejo, A. Tropical perturbations in the Eastern Pacific and the Precipitation field over North-Western Mexico in relation to the enso phenomenon. *Int. J. Climatol.* **1991**, *11*, 515–528. [[CrossRef](#)]
69. Seager, R.; Kushnir, Y.; Herweijer, C.; Naik, N.; Velez, J. Modeling of Tropical Forcing of Persistent Droughts and Pluvials over Western North America: 1856–2000. *J. Clim.* **2005**, *18*, 4065–4088. [[CrossRef](#)]
70. Martínez-Sánchez, J.N.; Cavazos, T. Eastern Tropical Pacific hurricane variability and landfalls on Mexican coasts. *Clim. Res.* **2014**, *58*, 221–234. [[CrossRef](#)]
71. Johnson, B.O.; Delworth, T.L. The Role of the Gulf of California in the North American Monsoon. *J. Clim.* **2023**, *36*, 1541–1559. [[CrossRef](#)]

Disclaimer/Publisher’s Note: The statements, opinions and data contained in all publications are solely those of the individual author(s) and contributor(s) and not of MDPI and/or the editor(s). MDPI and/or the editor(s) disclaim responsibility for any injury to people or property resulting from any ideas, methods, instructions or products referred to in the content.